

# Prediction of pseudogap formation due to $d$ -wave bond-order in organic superconductor $\kappa$ -(BEDT-TTF)<sub>2</sub>X

Rina Tazai<sup>1</sup>, Youichi Yamakawa<sup>1</sup>, Masahisa Tsuchiizu<sup>2</sup> and Hiroshi Kontani<sup>1</sup>

<sup>1</sup>*Department of Physics, Nagoya University, Furo-cho, Nagoya 464-8602, Japan.*

<sup>2</sup>*Department of Physics, Nara Women's University, Nara 630-8506, Japan.*

(Dated: April 10, 2024)

Rich hidden unconventional orders with pseudogap formation, such as the inter-site bond-order (BO), attract increasing attention in condensed matter physics. Here, we investigate the hidden order formation in organic unconventional superconductor  $\kappa$ -(BEDT-TTF)<sub>2</sub>X. We predict the formation of  $d$ -wave BO at wavelength  $\mathbf{q} = \mathbf{Q}_B = (\delta, \delta)$  ( $\delta = 0.38\pi$ ) for the first time, based on both the functional renormalization group (fRG) and the density-wave equation theories. The origin of the BO is the quantum interference among antiferromagnetic spin fluctuations. This prediction leads to distinct pseudogap-like reduction in the NMR  $1/T_1$  relaxation rate and in the density-of-states, consistently with essential experimental reports. The present theory would be applicable for other strongly correlated metals with pseudogap formation.

The layered organic compounds  $\kappa$ -(BEDT-TTF)<sub>2</sub>X attract considerable attention because of their rich variety of ground states due to strong electron correlation. Many compounds show the antiferromagnetic (AFM) insulating states at ambient pressure [1, 2], except for several quantum spin-liquid compounds (like X=Cu<sub>2</sub>(CN)<sub>3</sub>) [3]. Under pressure, many of them show unconventional superconductivity ( $T_c \gtrsim 10$ K) next to the AFM phase [1, 2]. In X=Cu[N(CN)<sub>2</sub>]Br and X=Cu(NCS)<sub>2</sub>, metallicity and superconductivity appear even at ambient pressure. Up to now,  $d_{x^2-y^2}$  and/or  $d_{xy}$  symmetries are predicted based on the spin-fluctuation mechanisms [4–8], the VMC study [9], and cluster DMFT study [10].

A central mystery in anomalous metallic states in  $\kappa$ -(BEDT-TTF)<sub>2</sub>X would be the origin of the pseudogap and its relation to the superconductivity. Both the NMR relaxation ratio  $1/T_1T$  [1, 2] and the density-of-states (DOS) measured by the STM [11] exhibit gap behaviors below  $T^* \sim 50$ K. As origins of the pseudogap, for example, crossover scenarios due to strong spin or superconducting (SC) fluctuations [12–20] and proximity effect to Mottness [21, 22] have been discussed. However, distinct kink-like changes observed in  $1/T_1T$  [1, 2] and in the hardening of optical phonon frequency [23] indicates the emergence of a hidden order parameter at  $T \approx T^*$ . (The intra-dimer charge disproportionation is reported only in X=Cu<sub>2</sub>(CN)<sub>3</sub> [9].)

The similarity between  $\kappa$ -(BEDT-TTF)<sub>2</sub>X and cuprate high- $T_c$  superconductors has been actively discussed for years. Recently, in many cuprates, the charge density-wave (DW) order in period  $3a \sim 4a$  at  $T_{CDW} \sim 200$ K has been discovered by the X-ray scattering, STM study, and NMR analysis [24–29]. In addition, nematic transition (presumably at  $\mathbf{q} = \mathbf{0}$ ) emerges at the pseudogap temperature  $T^*$  ( $> T_{CDW}$ ) [30–34]. These charge-channel phase transitions at  $T_{CDW}$  and  $T^*$  have been hotly discussed based on the charge/spin current order [35–37], and  $d$ -wave bond-order (BO) scenarios [38–48]. The BO is the modulation of correlated hopping integrals, and it can be

caused by the paramagnon interference mechanism [45–48] that is overlooked in usual spin fluctuation theories. This mechanism has also been applied to Fe-based superconductors [49–53] and heavy-fermion systems [54]. Thus, it is significant to study the paramagnon interference effects in  $\kappa$ -(BEDT-TTF)<sub>2</sub>X to go beyond the conventional understanding of this system.

In this paper, we discuss the occurrence of hidden charge DW orders in  $\kappa$ -(BEDT-TTF)<sub>2</sub>X by using both the functional renormalization group (fRG) and the DW equation methods. We predict the  $d$ -wave BO order formation at wavelength  $\mathbf{q} = \mathbf{Q}_B = (\delta, \delta)$  ( $\delta = 0.38\pi$ ) in  $\kappa$ -(BEDT-TTF)<sub>2</sub>X for the first time. The origin of the BO is novel quantum interference among paramagnons with  $\mathbf{Q}_S^\pm \approx (\pi \pm \delta/2, \pi \pm \delta/2)$ . The predicted distinct reductions in the spin fluctuation strength and in the DOS at BO transition temperature naturally explain the NMR and Raman measurements.

To analyze the quantum interference in low-dimensional metals, the fRG method is very powerful and reliable, since various DW instabilities (both particle-particle and particle-hole channels) are treated on the same footing [41, 46, 47, 55–59]. Using the fRG, unconventional DW states in cuprates and ruthenates have been analyzed satisfactorily [47, 58]. The fRG method is suitable to analyze the many-body electronic states, and we can obtain reliable results by making careful comparison with the diagrammatic calculation using the DW equation method [47, 51–53].

Here, we introduce the anisotropic triangular lattice dimer Hubbard model, which is the simplest effective model for  $\kappa$ -(BEDT-TTF)<sub>2</sub>X;  $\hat{H} = \hat{H}_0 + \hat{H}_U$  [60]. The kinetic term is given by  $\hat{H}_0 = \sum_{\mathbf{k}\sigma} \epsilon_{\mathbf{k}} c_{\mathbf{k}\sigma}^\dagger c_{\mathbf{k}\sigma}$  with  $\epsilon_{\mathbf{k}} = 2t(\cos k_x + \cos k_y) + 2t' \cos(k_x + k_y)$ . Indices  $\mathbf{k}$  and  $\sigma$  denote the momentum and spin, respectively. Here, we set the hopping integrals in Fig. 1 (a) as  $(t, t') = (-1, -0.5)$ . We verified that similar numerical results are obtained for  $t'/t = 0.5 \sim 0.8$ , which is realized in many compounds [61]. The on-site Coulomb interaction term is

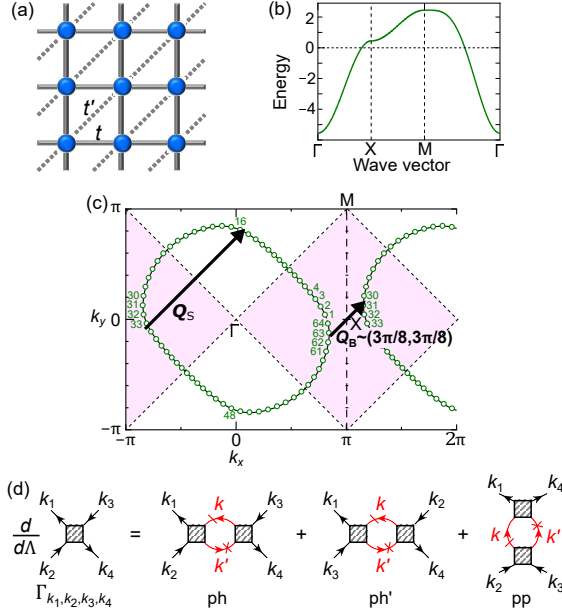


FIG. 1: (a) Anisotropic triangular lattice for  $\kappa$ -(BEDT-TTF) $_2$ X. (b) Band dispersion and (c) the FS at  $n = 1$ . The major nesting vector is  $\mathbf{Q}_S \approx (\pi - \delta/2, \pi - \delta/2)$  and the minor nesting vector is  $\mathbf{Q}_B \approx (\delta, \delta)$  with  $\delta \approx 3\pi/8$ . (d) Differential equation of the fRG theory. The crossed line represents electron propagator inside of the energy cutoff ( $|\epsilon_{\mathbf{k}'}| < \Lambda_l$ ), while the slashed line denotes on-shell one ( $|\epsilon_{\mathbf{k}}| = \Lambda_l$ ).

given by  $\hat{H}_U = \sum_{\mathbf{k}_1, \mathbf{k}_2, \mathbf{k}_3, \mathbf{k}_4} \frac{1}{4} \Gamma_{\mathbf{k}_1, \mathbf{k}_2, \mathbf{k}_3, \mathbf{k}_4}^0 c_{\mathbf{k}_1}^\dagger c_{\mathbf{k}_2} c_{\mathbf{k}_3} c_{\mathbf{k}_4}^\dagger \cdot \delta_{\mathbf{k}_1 - \mathbf{k}_2 - \mathbf{k}_3 + \mathbf{k}_4, \mathbf{0}}$ , where  $\mathbf{k}_i = (\mathbf{k}_i, \sigma_i)$  and  $\mathbf{0}$  is the zero vector in the reduced zone. The initial four-point vertex is  $\Gamma_{\mathbf{k}_1, \mathbf{k}_2, \mathbf{k}_3, \mathbf{k}_4}^0 = U(\delta_{\sigma_1, \sigma_3} \delta_{\sigma_2, \sigma_4} - \delta_{\sigma_1, \sigma_2} \delta_{\sigma_3, \sigma_4})$ . The four-point vertex acquires the momentum dependence after the renormalization, which is uniquely divided into the spin and charge parts as  $\Gamma_{\mathbf{k}_1, \mathbf{k}_2, \mathbf{k}_3, \mathbf{k}_4}^0 = \frac{1}{2} \Gamma_{\mathbf{k}_1, \mathbf{k}_2, \mathbf{k}_3, \mathbf{k}_4}^{0c} \delta_{\sigma_1, \sigma_2} \delta_{\sigma_3, \sigma_4} + \frac{1}{2} \Gamma_{\mathbf{k}_1, \mathbf{k}_2, \mathbf{k}_3, \mathbf{k}_4}^{0s} (\vec{\sigma})_{\sigma_1, \sigma_2} \cdot (\vec{\sigma})_{\sigma_3, \sigma_4}$ . The initial condition  $\Gamma^0s = -\Gamma^0c (= U)$  is largely modified by the renormalization.

In the following numerical study, we set the energy unit  $|t| = 1$ , and put the temperature  $T = 0.05$  and the electron filling  $n = 1$  ( $\mu = 0.55$ ). The band structure and the Fermi surface (FS) are presented in Figs. 1 (b) and (c), respectively. The patch indices ( $1 \sim 64$ ) are shown on the ellipsoid electron pockets. The total band width is  $W_D \sim 10$  (in unit  $|t| = 1$ ), and  $|t|$  corresponds to 0.05eV since  $W_D \sim 0.5$ eV experimentally [5, 60].

In the present study, we analyze the model by applying the RG+cRPA method developed in Refs. [46, 47, 58, 59], which is an efficient hybrid method between the fRG and the random-phase-approximation (RPA). Here, we introduce the higher-energy cutoff  $\Lambda_0 (= 2)$  and the logarithmic energy mesh  $\Lambda_l = \Lambda_0 e^{-l}$  with  $l \geq 0$ . Then, the effective four-point vertex  $\hat{\Gamma}$  is derived from the one-loop RG equation in Fig. 1 (d), by including the on-shell contribution  $\Lambda_{l+d} < |\epsilon_{\mathbf{k}} - \mu| \leq \Lambda_l$  step-by-step. In

strongly correlated systems,  $\hat{\Gamma}$  strongly deviates from  $\hat{\Gamma}^0$ . In this procedure, the Brillouin zone (BZ) is divided into  $N_p$  patches; see the Supplemental Materials (SM) A [62]. Below, we set  $\Lambda_0 = 2$  and  $N_p = 64$ . (Numerical results are not sensitive to the choices of  $\Lambda_0$  and  $N_p$ .) We analyze the higher energy region  $|\epsilon_{\mathbf{k}} - \mu| \geq \Lambda_0$ , where the vertex corrections (VCs) are less important, based on the constrained RPA (cRPA) with high numerical accuracy using fine  $\mathbf{k}$ -meshes. By using the RG+cRPA method, we can perform reliable calculations [46, 47, 58].

In Fig. 1 (d), the 3rd (1st and 2nd) term of r.h.s represents scattering process for particle-particle (pp) channel (particle-hole (ph) channels). The RG flow starts from  $l = 0$  ( $\Lambda_l = \Lambda_0$ ) to  $l \rightarrow \infty$  ( $\Lambda_l \rightarrow 0$ ). In the parallel way, we solve the RG equation for the susceptibilities [58]. The RG flow will stop for  $\Lambda_l \lesssim \omega_c$  with  $\omega_c = \max\{T, \gamma\}$ , where  $\gamma$  ( $\propto |\text{Im}\Sigma|$ ) is the quasiparticle damping rate. Considering large  $\gamma$  in  $\kappa$ -(BEDT-TTF) $_2$ X, we introduce the low-energy cutoff  $\omega_c = \pi T$  in the RG equation of the four-point vertex  $\Gamma$  in calculating Fig. 2 by following Refs. [46, 47].

Here, we show numerical results for the dimer Hubbard model. First, we calculate various DW susceptibilities at  $\omega = 0$  using the RG+cRPA method. The spin (charge) susceptibility with the form factor  $f_x(\mathbf{k})$  is [47]

$$\chi_x^{s(c)}(\mathbf{q}) = \int_0^\beta d\tau \frac{1}{2} \left\langle A_x^{s(c)}(\mathbf{q}, \tau) A_x^{s(c)}(-\mathbf{q}, 0) \right\rangle, \quad (1)$$

where  $A_x^{s(c)}(\mathbf{q}) \equiv \sum_{\mathbf{k}} f_x(\mathbf{k}) (c_{\mathbf{k}-\mathbf{q}/2\uparrow}^\dagger c_{\mathbf{k}+\mathbf{q}/2\uparrow} - (+) c_{\mathbf{k}-\mathbf{q}/2\downarrow}^\dagger c_{\mathbf{k}+\mathbf{q}/2\downarrow})$ . We calculate the spin and charge susceptibilities with the following form factors  $f_1 = 1$ ,  $f_x = \sqrt{2} \sin k_x$ ,  $f_y = \sqrt{2} \sin k_y$ ,  $f_{x^2-y^2} = \cos k_x - \cos k_y$  and  $f_{xy} = 2 \sin k_x \sin k_y$ . As a result, we find that the spin susceptibility  $\chi^S(\mathbf{q}) \equiv \chi_1^S(\mathbf{q})$  and the  $d_{x^2-y^2}$ -wave BO susceptibility  $\chi^{\text{BO}}(\mathbf{q}) \equiv \chi_{x^2-y^2}^c(\mathbf{q})$  strongly develop. Other susceptibilities remain small in the present study.

In Figs. 2 (a) and (b), we plot  $\mathbf{q}$ -dependences of  $\chi^S(\mathbf{q})$  and  $\chi^{\text{BO}}(\mathbf{q})$  at  $U = 3.5$ . Strong spin fluctuations develop at  $\mathbf{q} = \mathbf{Q}_S$ , consistently with the previous RPA and FLEX analyses [5]. In addition, we reveal the development of  $\chi^{\text{BO}}(\mathbf{q})$  at  $\mathbf{q} = \mathbf{Q}_B \approx (3\pi/8, 3\pi/8)$  in addition to  $\mathbf{q} = (0, 0)$ . The obtained strong bond fluctuations originate from the VCs that are dropped in the RPA.

The  $\chi^{\text{BO}}(\mathbf{q})$  strongly develops by increasing  $U$ . Figure 2 (c) shows the RG flow of the susceptibilities in the case of  $U = 3.54$ . In this case, the bond susceptibility exceeds the spin one after completing the renormalization. We see that  $\chi^S(\mathbf{Q}_S)$  starts to increase in the early stage of the renormalization, by reflecting the major nesting of the FS at  $\mathbf{q} = \mathbf{Q}_S$ . Next,  $\chi^{\text{BO}}(\mathbf{Q}_B)$  starts to increase for  $l \gtrsim 3$ , and it exceeds  $\chi^S(\mathbf{Q}_S)$  at  $l \sim 4$ . Finally,  $\chi^{\text{BO}}(\mathbf{0})$  starts to increase for  $l \gtrsim 4$  ( $\Lambda_l \lesssim 0.037$ ), because the renormalization of the Pauli ( $\mathbf{q} = \mathbf{0}$ ) susceptibility occurs only for  $\Lambda_l \lesssim T$ . All susceptibilities saturate for  $l \gtrsim 8$  ( $\Lambda_l \lesssim 0.7 \times 10^{-3}$ ). The final results in Figs. 2 (a)

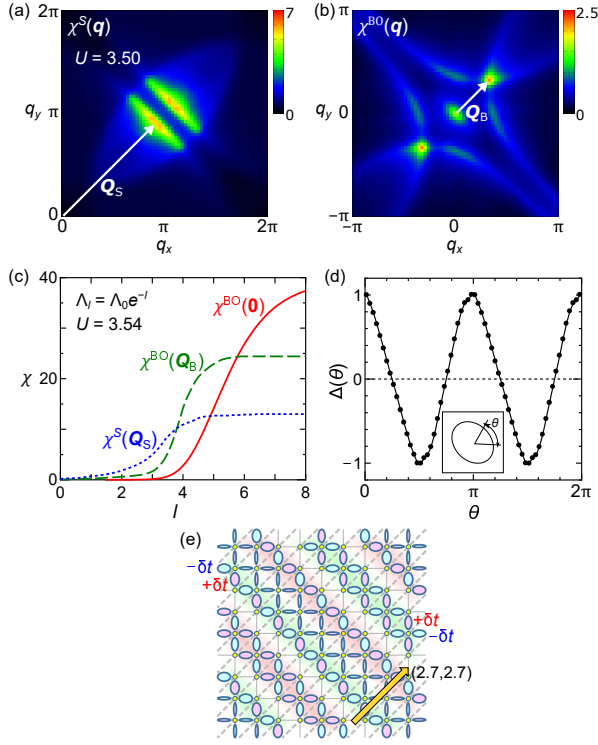


FIG. 2: The  $\mathbf{q}$ -dependences of (a)  $\chi^S(\mathbf{q})$  and (b)  $\chi^{BO}(\mathbf{q})$  obtained by the RG+cRPA method at  $U = 3.5$ . (c) The RG flow for spin and BO susceptibilities at  $U = 3.54$ . (d) Obtained optimized SC gap function, which belongs to  $d_{x^2-y^2}$ -wave symmetry. (e) Schematic BO pattern at  $\mathbf{q} = \mathbf{Q}_B$  in the real space, where  $\boldsymbol{\lambda} \approx (8/3, 8/3)$  is the wavevector.

and (b) are given at  $l \approx 9$ . Thus, all  $\chi^S(\mathbf{Q}_S)$ ,  $\chi^{BO}(\mathbf{Q}_B)$  and  $\chi^{BO}(\mathbf{0})$  strongly develop at  $U = 3.54$ .

We also calculate the spin-singlet SC susceptibility [47]

$$\chi^{SC} = \frac{1}{2} \int_0^\beta d\tau \langle B^\dagger(\tau) B(0) \rangle, \left( B \equiv \sum_{\mathbf{k}} \Delta(\mathbf{k}) c_{\mathbf{k}\uparrow} c_{-\mathbf{k}\downarrow} \right) \quad (2)$$

where  $\Delta(\mathbf{k})$  is an even parity gap function, which is uniquely determined so as to maximize  $\chi^{SC}$  under the constraint  $\frac{1}{N} \sum_{\mathbf{k}} |\Delta(\mathbf{k})|^2 \delta(\epsilon_{\mathbf{k}} - \mu) = 1$  [47]. We show the obtained optimized gap at  $U = 3.54$  in Fig. 2 (d). The obtained gap function in the  $d_{x^2-y^2}$ -wave symmetry is understood as the spin-fluctuation-mediated  $d$ -wave state [5]. In the present case, large BO susceptibilities  $\chi^{BO}(\mathbf{Q}_B)$  and  $\chi^{BO}(\mathbf{0})$  should contribute to the pairing mechanism (see Fig. 3 (b)).

Figure 2 (e) shows the schematic  $d$ -wave BO pattern at  $\mathbf{q} = \mathbf{Q}_B$ . Here, each red (blue) ellipse represents the increment (decrement) of the hopping integral  $\delta t_\mu$  ( $\mu = x, y$ ) caused by the BO parameters. The opposite sign between the adjacent  $\delta t_x$  and  $\delta t_y$  reflects the  $d$ -wave symmetry of the BO. The BO parameter causes the pseudogap in the DOS (see Figs. 4 (d) and (e)).

Now, we clarify the importance of the spin fluctuations on the BO fluctuations. For this purpose, we solve the

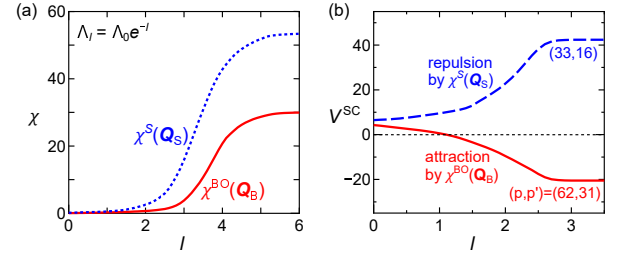


FIG. 3: Obtained RG results in the case of  $\omega_c^{pp} = 10T$  at  $U = 3.82$ . (a) Obtained RG flow for  $\chi^{BO}(\mathbf{Q}_B)$  and  $\chi^S(\mathbf{Q}_S)$ . (b) Obtained pairing interaction  $V^{SC}(\mathbf{p}, \mathbf{p}')$  due to the spin-fluctuation-mediated repulsion (for  $(\mathbf{p}, \mathbf{p}') = (33, 16)$ ) and the BO fluctuation-mediated attraction (for  $(\mathbf{p}, \mathbf{p}') = (62, 31)$ ). The patch number  $\mathbf{p}$  and  $\mathbf{p}'$  are shown in Fig. 1 (c).

RG equation by dropping the contribution from the pp channel in the RG equation for  $\Gamma$ , by introducing an additional cutoff energy only for the pp channel;  $\omega_c^{pp} (> \omega_c)$ . Here, we set  $\omega_c^{pp} = 10T$  to suppress the SC fluctuations selectively. The obtained RG flows of the susceptibilities at  $U = 3.82$  are shown in Fig. 3 (a). We see that  $\chi^S(\mathbf{Q}_S)$  starts to increase in the early stage, due to the ph channels in the RG equations in Fig. 1 (d). Next,  $\chi^{BO}(\mathbf{Q}_B)$  also increases to follow the increment of  $\chi^S(\mathbf{Q}_S)$ , similarly to Fig. 2 (c). This result strongly indicates that the BO fluctuations are driven by the spin fluctuations. Note that  $\chi^{BO}(\mathbf{Q}_B)$  exceeds  $\chi^S(\mathbf{Q}_S)$  by setting  $U = 3.86$  even in the case  $\omega_c^{pp} = 10T$ .

Next, we discuss the SC pairing vertex function  $V^{SC}(\mathbf{p}, \mathbf{p}') = \frac{3}{2}\Gamma^s(\mathbf{p}, \mathbf{p}', -\mathbf{p}', -\mathbf{p}) - \frac{1}{2}\Gamma^c(\mathbf{p}, \mathbf{p}', -\mathbf{p}', -\mathbf{p}) - \Gamma^{0s}$  given by the RG+cRPA method [59]. Due to large  $\omega_c^{pp} (= 10T)$ , the obtained  $V^{SC}(\mathbf{p}, \mathbf{p}')$  becomes “irreducible with respect to the pp channel” below  $\omega_c^{pp}$ . Then,  $V^{SC}(\mathbf{p}, \mathbf{p}')$  gives the “pairing interaction in the SC gap equation” with the BCS cutoff energy  $\omega_{BCS} = \omega_c^{pp}$ . The obtained RG flow of  $V^{SC}(\mathbf{p}, \mathbf{p}')$  is shown in Fig. 3 (b). The large repulsion for  $\mathbf{p} - \mathbf{p}' \approx \mathbf{Q}_S$  is apparently given by the spin fluctuations. Interestingly, we find that the attraction for  $\mathbf{p} - \mathbf{p}' \approx \mathbf{Q}_B$  is caused by the BO fluctuations in Fig. 3 (a). The present result indicates that both  $\chi^{BO}(\mathbf{Q}_B)$  and  $\chi^S(\mathbf{Q}_S)$  cooperatively work as the pairing glue of the  $d_{x^2-y^2}$ -wave state, as understood in Fig. 1 (c). The obtained gap structure is very similar to Fig. 2 (d). Therefore, the  $d$ -wave BO fluctuations in the single-orbital Hubbard model can mediate large attractive pairing interaction.

Next, we explain that the BO fluctuations originate from the quantum interference between paramagnons, which is described by the Aslamazov-Larkin (AL) quantum process. For this purpose, we analyze the following DW equation [48, 51–53]:

$$\lambda_{\mathbf{q}}^{DW} f_{\mathbf{q}}(k) = -\frac{T}{N} \sum_{k'} I_{\mathbf{q}}^c(k, k') G(k_-') G(k_+') f_{\mathbf{q}}(k'), \quad (3)$$

where  $\lambda_{\mathbf{q}}^{DW}$  is the eigenvalue that represents the charge

channel DW instability at wavevector  $\mathbf{q}$ . Here,  $\mathbf{p}_\pm \equiv \mathbf{p} \pm \mathbf{q}/2$ , and  $k \equiv (\mathbf{k}, \epsilon_n)$  and  $p \equiv (\mathbf{p}, \epsilon_m)$  ( $\epsilon_n, \epsilon_m$  are fermion Matsubara frequencies). The eigenfunction  $f_{\mathbf{q}}(\mathbf{k})$  gives the form factor. The corresponding DW susceptibility is  $\chi^{\text{BO}} \propto (1 - \lambda_{\mathbf{q}}^{\text{DW}})^{-1}$ . In the present model, the obtained DW state corresponds to the  $d$ -wave BO.

The kernel function  $I^c$  is given by the Ward identity  $-\delta\Sigma/\delta G$ , which is composed of one single-paramagnon exchange term and two double-paramagnon exchange ones: The former and the latter are called the Maki-Thompson (MT) term and the AL terms; see Fig. 4 (a). (Each wavy line is proportional to  $\chi^S(\mathbf{q})$ .) Among four terms in  $I_{\mathbf{q}}^c$ , the AL terms are significant for  $\alpha_S \lesssim 1$ , and they give spin-fluctuation-driven nematic orders in cuprates and Fe-based superconductors [48, 49].

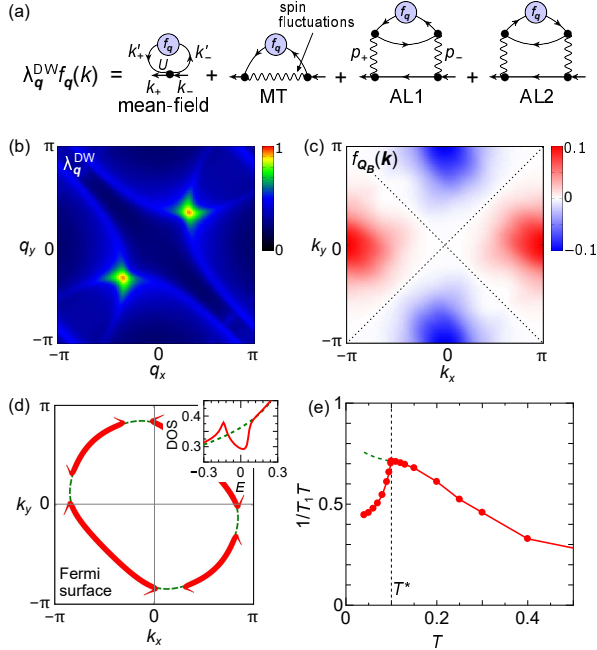


FIG. 4: (a) The DW equation for wavevector  $\mathbf{q}$ .  $\mathbf{k}_\pm \equiv \mathbf{k} \pm \mathbf{q}/2$  and  $\mathbf{p}_\pm \equiv \mathbf{p} \pm \mathbf{q}/2$ . The kernel function is composed of the mean-field, MT, and AL1,2 terms. These diagrams are also produced systematically by solving the RG equation. (b) Obtained eigenvalue of the BO  $\lambda_{\mathbf{q}}^{\text{DW}}$  and (c) the form factor  $f_{\mathbf{q}}(\mathbf{k})$  at  $\mathbf{q} = \mathbf{Q}_B$  and  $\epsilon_n = \pi T$ . (d) Obtained Fermi arc structure in the unfolded zone, and the pseudogap in the DOS with  $f^{\text{max}} = 0.1$  is shown in the inset. (e) Obtained  $1/T_1 T$ , where  $T^*$  is the BO transition temperature.

Figure 4 (b) shows the obtained eigenvalue of the BO,  $\lambda_{\mathbf{q}}^{\text{DW}}$ , at  $T = 0.05$  and  $U = 2.53$ , where the Stoner factor  $\alpha_S = U\chi^0(\mathbf{Q}_S)$  is 0.90. Here,  $\chi^0(\mathbf{q})$  is the irreducible susceptibility, and the SDW occurs when  $\alpha_S = 1$ . The eigenvalue  $\lambda_{\mathbf{q}}^{\text{DW}}$  reaches almost unity at  $\mathbf{q} = \mathbf{Q}_B$ , which is consistent with  $\chi^{\text{BO}}(\mathbf{q})$  given by the RG+cRPA in Fig. 2 (b). The corresponding form factor in Fig. 4 (c) possesses the  $d_{x^2-y^2}$ -wave symmetry. Therefore, strong  $d_{x^2-y^2}$ -wave BO susceptibility at  $\mathbf{q} = \mathbf{Q}_B$  by the RG+cRPA method in Fig. 2 (b) is well reproduced by the DW equa-

tion. The origin of the strong BO instability at  $\mathbf{q} = \mathbf{Q}_B$  is the AL terms in Fig. 4 (a) that represent the quantum interference among paramagnons at  $\mathbf{Q}_S^\pm \approx (\pi, \pi) \pm \mathbf{Q}_B/2$ . (Note that  $\chi^S(\mathbf{q})$  given by the RPA is similar to that the fRG result in Fig. 2 (a).)

The paramagnon-interference mechanism can generate both the ferro-BO instability (at  $\mathbf{q} = \mathbf{Q}_S^+ - \mathbf{Q}_S^- = \mathbf{0}$ ) and the incommensurate-BO one (at  $\mathbf{q} = \mathbf{Q}_S^+ - \mathbf{Q}_S^- = \mathbf{Q}_B$ ). This mechanism causes the ferro-BO states in both Fe-based and cuprate superconductors according to the DW equation analysis [48, 51–53]. In the present dimer Hubbard model, in contrast, the ferro-BO fluctuations remain small in the DW equation analysis. This is also true in the fRG analysis with  $\omega_c^{\text{pp}} = 10T$  shown in Fig. 3. These results indicate that the paramagnon interference mechanism alone is not sufficient to establish large  $\chi^{\text{BO}}(\mathbf{0})$  in Fig. 2 (b). Therefore, we conclude that large  $\chi^{\text{BO}}(\mathbf{0})$  is caused by the spin and SC fluctuations cooperatively, since the AL processes by SC fluctuations can cause the ferro-BO fluctuations according to Ref. [58].

Finally, we discuss the band-folding and hybridization gap due to the BO with  $\mathbf{q} = \mathbf{Q}_B$ . Figure 4 (d) shows the Fermi arc structure obtained for  $f^{\text{max}} \equiv \max_{\mathbf{k}} \{f_{\mathbf{Q}_B}(\mathbf{k})\} = 0.1$ . Here, the folded band structure under the BO at  $\mathbf{q} = \mathbf{Q}_B$  is “unfolded” into the original Brillouin zone [63] to make a comparison with ARPES experiment. The resultant pseudogap in the DOS is shown in the inset of Fig. 4 (d), which is consistent with the STM study [11]. The BO leads to significant reduction of the spin fluctuation strength, so the obtained  $1/T_1 T \propto \sum_{\mathbf{q}, \alpha, \beta} \text{Im} \chi_{\alpha, \beta}^s(\mathbf{q}, \omega)/\omega|_{\omega=0}$  shown in Fig. 4 (e) exhibit kink-like pseudogap behavior. Here,  $\alpha, \beta$  represent the sites in the unit cell under the presence of the BO, and we set  $f^{\text{max}} = 0.2 \times \tanh(1.74\sqrt{(1 - T/T^*)})$  below the BO transition temperature  $T^* = 0.1$ . (Here,  $2f^{\text{max}}(T = 0)/T^* = 4$ .) The obtained pseudogap behaviors in  $1/T_1 T$  and DOS are consistent with phase-transition-like experimental behaviors [1, 2, 23].

In the fRG study, the parquet VCs are generated by considering all ph, ph’ and pp channels in Fig. 1 (d). On the other hand, in the DW equation study, the VCs are limited to MT and AL terms, whereas their frequency dependences are calculated correctly. Both theoretical methods lead to the emergence of the *same*  $d$ -wave bond order shown in Fig. 2 (e).

In summary, we predicted the emergence of the  $d$ -wave BO at wavevector  $\mathbf{q} = \mathbf{Q}_B = (0.38\pi, 0.38\pi)$  in  $\kappa$ -(BEDT-TTF)<sub>2</sub>X, due to the interference between paramagnons with  $\mathbf{Q}_S^\pm \approx (\pi, \pi) \pm \mathbf{Q}_B/2$ . The BO is derived from both fRG method and the DW equation method. The BO transition leads to distinct pseudogap behaviors in the NMR  $1/T_1$  relaxation rate and in the DOS, consistently with many experimental reports at  $T \approx T^*$ . As we show in the SM B [62], very similar numerical results are obtained in the case of  $t'/t = 0.7$ . Thus, the  $d$ -wave BO will



be ubiquitous in  $\kappa$ -(BEDT-TTF)<sub>2</sub>X. The present theory would be applicable for other strongly correlated metals with pseudogap formation.

We are grateful to S. Onari for useful discussions. This work is supported by Grants-in-Aid for Scientific Research (KAKENHI) Research (No. JP20K22328, No. JP20K03858, No. JP19H05825, No. JP18H01175, JP16K05442) from MEXT of Japan.

- 
- [1] K. Kanoda, *Physica C* **282-287**, 299 (1997).
  - [2] K. Kanoda and R. Kato, *Annu. Rev. Condens. Matter Phys.* **2**, 167 (2011).
  - [3] Y. Shimizu, K. Miyagawa, K. Kanoda, M. Maesato, and G. Saito *Phys. Rev. Lett.* **91**, 107001 (2003).
  - [4] J. Schmalian: *Phys. Rev. Lett.* **81**, 4232 (1998).
  - [5] H. Kino and H. Kontani: *J. Phys. Soc. Jpn.* **67**, 3691 (1998).
  - [6] H. Kondo and T. Moriya: *J. Phys. Soc. Jpn.* **67**, 3695 (1998).
  - [7] H. Kontani and H. Kino, *Phys. Rev. B* **63**, 134524 (2001).
  - [8] K. Kuroki, *J. Phys. Soc. Jpn.* **75**, 051013 (2006).
  - [9] H. Watanabe, H. Seo, and S. Yunoki, *Nat. Commun.* **10**, 3167 (2019).
  - [10] B. Kyung and A. M. S. Tremblay, *Phys. Rev. Lett.* **97**, 046402 (2006).
  - [11] T. Arai, K. Ichimura, K. Nomura, S. Takasaki, J. Yamada, S. Nakatsuji, and H. Anzai, *Solid State Commun.* **116**, 679 (2000).
  - [12] T. Kobayashi, Y. Ihara, Y. Saito, and A. Kawamoto, *Phys. Rev. B* **89**, 165141 (2014).
  - [13] Y. Eto, M. Itaya, and A. Kawamoto, *Phys. Rev. B* **81**, 212503 (2010).
  - [14] S. Tsuchiya, K. Nakagawa, J. Yamada, H. Taniguchi, and Y. Toda, *Phys. Rev. B* **96**, 134311 (2017).
  - [15] K. Nakagawa, S. Tsuchiya, J. Yamada, and Y. Toda, *Europhys. Lett.* **122**, 67003 (2018).
  - [16] H. Kontani, *Rep. Prog. Phys.* **71**, 026501 (2008).
  - [17] Y. Yanase T. Jujo, T. Nomura, H. Ikeda, T. Hotta, and K. Yamada, *Phys. Rep.* **387**, 1 (2003).
  - [18] T. Moriya and K. Ueda, *Adv. Phys.* **49**, 555 (2000).
  - [19] J. Schmalian, D. Pines, and B. Stojkovic, *Phys. Rev. Lett.* **80**, 3839 (1998).
  - [20] B. Kyung, V. Hankevych, A. M. Dare, and A. M. S. Tremblay *Phys. Rev. Lett.* **93**, 147004 (2004).
  - [21] F. Kagawa, K. Miyagawa, and K. Kanoda, *Nature* **436**, 534 (2005).
  - [22] J. Kang, S.-L. Yu, T. Xiang, and J.-X. Li, *Phys. Rev. B* **84**, 064520 (2011).
  - [23] M. Revelli Beaumont, P. Hemme, Y. Gallais, A. Sacuto, K. Jacob, L. Valade, D. de Caro, C. Faulmann, and M. Cazayous, *J. Phys.: Condens. Matter* **33**, 125403 (2021).
  - [24] G. Ghiringhelli, M. L. Tacon, M. Minola, S. Blanco-Canosa, C. Mazzoli, N. B. Brookes, G. M. D. Luca, A. Frano, D. G. Hawthorn, F. He, T. Loew, M. M. Sala, D. C. Peets, M. Salluzzo, E. Schierle, R. Sutarto, G. A. Sawatzky, E. Weschke, B. Keimer, and L. Braicovich, *Science* **337**, 821 (2012).
  - [25] R. Comin, A. Frano, M. M. Yee, Y. Yoshida, H. Eisaki, E. Schierle, E. Weschke, R. Sutarto, F. He, A. Soumya-narayanan, Y. He, M. L. Tacon, I. S. Elfimov, J. E. Hoffman, G. A. Sawatzky, B. Keimer, and A. Damascelli, *Science* **343**, 390 (2014).
  - [26] Y. Kohsaka, T. Hanaguri, M. Azuma, M. Takano, J. C. Davis, and H. Takagi, *Nature Physics* **8**, 534 (2012).
  - [27] K. Fujita, M. H. Hamidian, S. D. Edkins, C. K. Kim, Y. Kohsaka, M. Azuma, M. Takano, H. Takagi, H. Eisaki, S. Uchida, A. Allais, M. J. Lawler, E.-A. Kim, S. Sachdev, and J. C. S. Davis, *Proc. Natl. Acad. Sci. USA*, **111**, E3026 (2014).
  - [28] T. Wu, H. Mayaffre, S. Krämer, M. Horvatić, C. Berthier, P. L. Kuhns, A. P. Reyes, R. Liang, W. N. Hardy, D. A. Bonn, and M.-H. Julien, *Nat. Comms.* **4**, 2113 (2013).
  - [29] T. Wu, H. Mayaffre, S. Krämer, M. Horvatić, C. Berthier, W. N. Hardy, R. Liang, D. A. Bonn, and M.-H. Julien, *Nat. Comms.* **6**, 1 (2015).
  - [30] Y. Sato, S. Kasahara, H. Murayama, Y. Kasahara, E.-G. Moon, T. Nishizaki, T. Loew, J. Porras, B. Keimer, T. Shibauchi, and Y. Matsuda, *Nature Physics* **13**, 1074 (2017).
  - [31] H. Murayama, Y. Sato, R. Kurihara, S. Kasahara, Y. Mizukami, Y. Kasahara, H. Uchiyama, A. Yamamoto, E.-G. Moon, J. Cai, J. Freyermuth, M. Greven, T. Shibauchi, and Y. Matsuda, *Nat. Commun.* **10**, 3282 (2019).
  - [32] S. Nakata, M. Horio, K. Koshiishi, K. Hagiwara, C. Lin, M. Suzuki, S. Ideta, K. Tanaka, D. Song, Y. Yoshida, H. Eisaki, and A. Fujimori, arXiv:1811.10028.
  - [33] K. Ishida, S. Hosoi, Y. Teramoto, T. Usui, Y. Mizukami, K. Itaka, Y. Matsuda, T. Watanabe, and T. Shibauchi, *J. Phys. Soc. Jpn.* **89**, 064707 (2020).
  - [34] W. Wang, J. Luo, C. G. Wang, J. Yang, Y. Kodama, R. Zhou, and G.-q. Zheng, arXiv:2008.12012.
  - [35] C. M. Varma, *Phys. Rev. B* **55**, 14554 (1997).
  - [36] H. Yokoyama, S. Tamura, and M. Ogata, *J. Phys. Soc. Jpn.* **85**, 124707 (2016).
  - [37] H. Kontani, Y. Yamakawa, R. Tazai, and S. Onari, arXiv:2003.07556
  - [38] S. Bulut, W.A. Atkinson and A.P. Kampf, *Phys. Rev. B* **88**, 155132 (2013).
  - [39] Y. Wang and A.V. Chubukov, *Phys. Rev. B* **90**, 035149 (2014).
  - [40] R.-Q. Xing, L. Classen, and A. V. Chubukov, *Phys. Rev. B* **98**, 041108(R) (2018).
  - [41] T. Holder and W. Metzner, *Phys. Rev. B* **85**, 165130 (2012).
  - [42] M.A. Metlitski and S. Sachdev, *New J. Phys.* **12**, 105007 (2010); S. Sachdev and R. La Placa, *Phys. Rev. Lett.* **111**, 027202 (2013).
  - [43] J. C. S. Davis and D.-H. Lee, *Proc. Natl. Acad. Sci. USA*, **110**, 17623 (2013).
  - [44] E. Berg, E. Fradkin, S. A. Kivelson, and J. M. Tranquada, *New J. Phys.* **11**, 115004 (2009).
  - [45] Y. Yamakawa, and H. Kontani, *Phys. Rev. Lett.* **114**, 257001 (2015).
  - [46] M. Tsuchiizu, Y. Yamakawa, and H. Kontani, *Phys. Rev. B* **93**, 155148 (2016).
  - [47] M. Tsuchiizu, K. Kawaguchi, Y. Yamakawa, and H. Kontani, *Phys. Rev. B* **97**, 165131 (2018).
  - [48] K. Kawaguchi, Y. Yamakawa, M. Tsuchiizu, and H. Kontani, *J. Phys. Soc. Jpn.* **86**, 063707 (2017).
  - [49] S. Onari and H. Kontani, *Phys. Rev. Lett.* **109**, 137001 (2012).
  - [50] Y. Yamakawa, S. Onari, and H. Kontani, *Phys. Rev. X* **6**, 021032 (2016).

- [51] S. Onari, Y. Yamakawa, and H. Kontani, Phys. Rev. Lett. **116**, 227001 (2016).
- [52] S. Onari and H. Kontani, Phys. Rev. B **100**, 020507(R) (2019).
- [53] S. Onari and H. Kontani, Phys. Rev. Research **2**, 042005(R) (2020).
- [54] R. Tazai and H. Kontani, Phys. Rev. B **100**, 241103(R) (2019).
- [55] W. Metzner, M. Salmhofer, C. Honerkamp, V. Meden, and K. Schönhammer, Rev. Mod. Phys. **84**, 299 (2012).
- [56] C. Honerkamp, Phys. Rev. B **72**, 115103 (2005).
- [57] C. Husemann and W. Metzner, Phys. Rev. B **86**, 085113 (2012).
- [58] M. Tsuchiizu, Y. Ohno, S. Onari, and H. Kontani, Phys. Rev. Lett. **111**, 057003 (2013).
- [59] R. Tazai, Y. Yamakawa, M. Tsuchiizu, and H. Kontani, Phys. Rev. B **94**, 115155 (2016).
- [60] H.Kino and H.Fukuyama, J. Phys. Soc. Jpn. **65**, 2158 (1996), and references therein.
- [61] B. J. Powell and R. H. McKenzie, Rep. Prog. Phys. **74**, 056501 (2011).
- [62] Supplemental Materials.
- [63] W. Ku, T. Berlijn, and C.-C. Lee, Phys. Rev. Lett. **104**, 216401 (2010).

[Supplementary Material]

**Prediction of  $d$ -wave bond-order and pseudogap in organic superconductor  $\kappa$ -(BEDT-TTF) $_2$ X: Similarities to cuprate superconductors**

Rina Tazai<sup>1</sup>, Youichi Yamakawa<sup>1</sup>, Masahisa Tsuchiizu<sup>2</sup> and Hiroshi Kontani<sup>1</sup>

<sup>1</sup>*Department of Physics, Nagoya University, Furo-cho, Nagoya 464-8602, Japan.*

<sup>2</sup>*Department of Physics, Nara Women's University, Nara 630-8506, Japan.*

**A: RG+cRPA METHOD FOR THE DIMER HUBBARD MODEL OF  $\kappa$ -(BEDT-TTF) $_2$ X**

In the main text, we studied the dimer Hubbard model, which is the simplest effective model for  $\kappa$ -(BEDT-TTF) $_2$ X, by applying the RG+cRPA method. This is a useful hybrid method between the fRG theory and the RPA developed in Ref. [1]. The RG+cRPA method is applicable for systems with complex valence-band structure, even when the conventional patch RG method is not applicable. Here, we solve the one-loop RG equation for the four-point vertex  $\Gamma$  in Fig. 1 (d) inside the energy region  $|\epsilon_{\mathbf{k}} - \mu| \leq \Lambda_0$ , by applying the logarithmic energy mesh  $\Lambda_l = \Lambda_0 e^{-l}$  with  $l \geq 0$ . In the framework of the  $N_p$ -patch RG, the lower-energy region in the Brillouin zone (BZ) is divided into  $N_p$  patches, as shown in Fig. S1 with  $\Lambda_0 = 2$  and  $N_p = 32$ . (Note that the numerical study in the main text is done for  $N_p = 64$ .) By solving the RG equation, we can calculate the vertex corrections (VCs), which are the many-body effects that are dropped in the RPA.

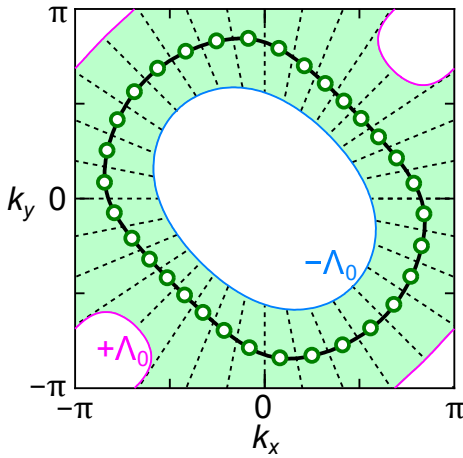


FIG. S1: The FS and the BZ of the present dimer model. The green shaded region  $|\epsilon_{\mathbf{k}} - \mu| \leq \Lambda_0 = 2$  is divided into  $N_p$  ( $= 32$ ) patches. The center of each patch on the FS is shown as small circle.

For the higher energy region  $|\epsilon_{\mathbf{k}} - \mu| \leq \Lambda_0$ , where the VCs are less important, we apply the constrained random-phase-approximation (cRPA) with high numeri-

cal accuracy using fine  $\mathbf{k}$ -meshes. The obtained effective interaction by cRPA is incorporated into the initial parameters of the fRG equation, without worrying about the double counting of diagrams. In solving the RG equation, we calculate the pp and ph scattering processes that include (at least) one on-shell state ( $\Lambda_l > \epsilon_{\mathbf{k}} > \Lambda_{l+dl}$ ) step-by-step, till the parameter  $l$  reaches  $\ln(\Lambda_0/\omega_c)$ . In the main text, we set  $\omega_c = \pi T$  in the RG equation for  $\Gamma$ , and  $\omega_c = T/100$  in the RG equations for the three-point vertex and the susceptibility. By using the RG+cRPA method, we can perform reliable numerical calculations [1–3]. The obtained numerical results are essentially robust against the choice of  $\Lambda_0$ .

**B:  $d$ -WAVE BO SOLUTIONS IN THE DIMER HUBBARD MODEL WITH  $t'/t = 0.7$**

In the main text, we examined the electronic states in the dimer Hubbard model with  $t'/t = 0.5$ . However, the ratio  $t'/t$  in  $\kappa$ -(BEDT-TTF) $_2$ X depends on the anion molecule X. In many compounds, the relation  $t'/t = 0.5 \sim 0.7$  is realized, except for the spin liquid compound X=Cu<sub>2</sub>(CN)<sub>3</sub> with  $t'/t \approx 1$ . In our previous study [4], experimental AFM-superconducting phase diagram is reproduced for  $t'/t = 0.5 \sim 0.8$ , by setting the ratio  $U/|t|$  larger for larger  $t'/t$ .

Here, we analyzed the dimer Hubbard model with  $t'/t = 0.7$  in order to verify the robustness of the  $d$ -wave BO against the modification of the model parameters. The Fermi surface (FS) for  $t'/t = 0.7$  is shown in Fig. S2 (a). The spin susceptibility and  $d$ -wave BO susceptibility obtained by the RG+cRPA method are shown in Figs. S2 (b) and (c), respectively, in the case of  $U = 4.10$  at  $T = 0.05$ . Since  $\chi^{\text{BO}}(\mathbf{q})$  remains very small in the RPA (FLEX), the obtained strong BO fluctuations in Fig. S2 (c) originate from the VCs that are dropped in the RPA (FLEX). The BO susceptibility strongly develops with increasing  $U$ , and it exceeds the spin susceptibility for  $U \geq 4.12$ .

Next, we perform the DW equation analysis for  $t'/t = 0.70$ . Then, the RPA spin susceptibility is shown in Fig. S3 (a) for  $U = 3.10$  at  $T = 0.05$ , where the Stoner factor  $\alpha_S = U\chi^0(\mathbf{Q}_S)$  is 0.90. Figure S3 (b) is the obtained eigenvalue of the DW equation. The derived form factor

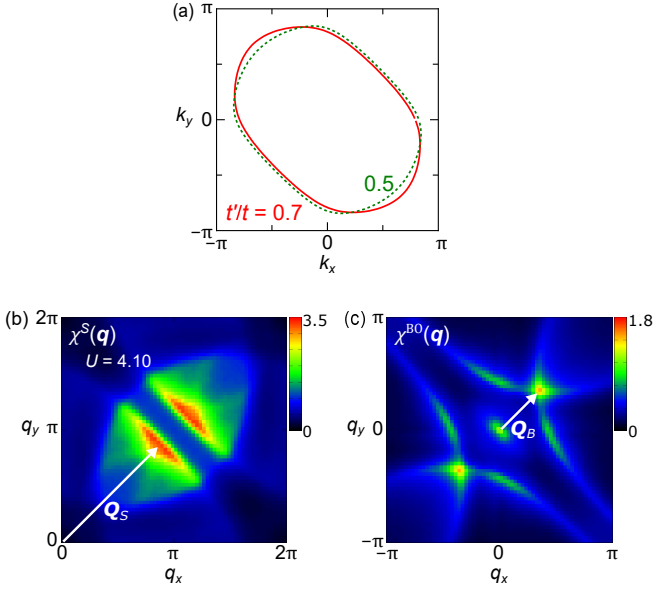


FIG. S2: (a) FS of the dimer model for  $t'/t = 0.7$ . We also show the FS for  $t'/t = 0.5$ , which is used in the main text. (b)  $\chi^S(\mathbf{q})$  and (c)  $\chi^{\text{BO}}(\mathbf{q})$  obtained by the RG+cRPA method for  $U = 4.10$  in the case of  $t'/t = 0.7$ . The obtained  $\chi^{\text{BO}}(\mathbf{q})$  has the peak structures at both  $\mathbf{q} = \mathbf{0}$  and  $\mathbf{Q}_B$ .

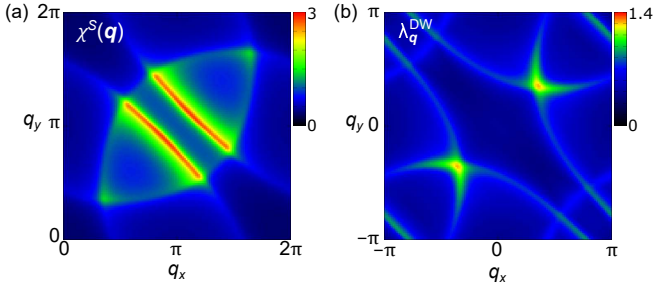


FIG. S3: (a)  $\chi^S(\mathbf{q})$  and (b)  $\lambda^{\text{DW}}(\mathbf{q})$  obtained by the DW equation for  $U = 3.10$  in the case of  $t'/t = 0.7$ .

at  $\mathbf{q} = \mathbf{Q}_B$  is very similar to the  $d_{x^2-y^2}$ -wave form factor for  $t'/t = 0.5$  obtained in Fig. 4 (c) in the main text. These results are essentially similar to the results by the RG+cRPA method in Fig. S2, except for the absence of the peak at  $\mathbf{q} = \mathbf{0}$  in Fig. S3 (b).

In summary, the development of the  $d$ -wave BO susceptibility at  $\mathbf{q} = \mathbf{Q}_B$ ,  $\chi^{\text{BO}}(\mathbf{Q}_B)$ , is confirmed by both the fRG theory and the DW equation theory in the dimer Hubbard model, in the cases of  $t'/t = 0.5$  and  $0.7$ . This result is derived from the AL-type VCs, which are neglected in the RPA. Since  $\lambda_{\mathbf{q}=\mathbf{0}}^{\text{DW}}$  in Fig. S3 (b) remains small, the enhancement of  $\chi^{\text{BO}}(\mathbf{0})$  in Fig. S3 (c) originates from the spin and SC fluctuations cooperatively, as we discussed in the main text.

Finally, it should be stressed that the ferro-BO can be induced by the paramagnon-interference mechanism in general systems. In fact, strong ferro-BO fluctuations observed in both Fe-based and cuprate superconductors are satisfactorily reproduced by the DW equation analysis [5–7], meaning that the ferro-BO fluctuations originate solely from the spin fluctuations.

- 
- [1] M. Tsuchiizu, Y. Ohno, S. Onari, and H. Kontani, Phys. Rev. Lett. **111**, 057003 (2013).
  - [2] M. Tsuchiizu, Y. Yamakawa, and H. Kontani, Phys. Rev. B **93**, 155148 (2016).
  - [3] M. Tsuchiizu, K. Kawaguchi, Y. Yamakawa, and H. Kontani, Phys. Rev. B **97**, 165131 (2018).
  - [4] H. Kino and H. Kontani: J. Phys. Soc. Jpn. **67**, 3691 (1998).
  - [5] K. Kawaguchi, Y. Yamakawa, M. Tsuchiizu, and H. Kontani, J. Phys. Soc. Jpn. **86**, 063707 (2017).
  - [6] S. Onari, Y. Yamakawa, and H. Kontani, Phys. Rev. Lett. **116**, 227001 (2016).
  - [7] S. Onari and H. Kontani, Phys. Rev. B **100**, 020507(R) (2019).